Anisotropic Lithiation Onset in Silicon Nanoparticle Anode Revealed by *in Situ* Graphene Liquid Cell Electron Microscopy

Jong Min Yuk,[†,‡,⊥,#] Hyeon Kook Seo,[†,‡,⊥] Jang Wook Choi,[§,*] and Jeong Yong Lee[†,‡,*]

[†]Center for Nanomaterials and Chemical Reactions, Institute for Basic Science (IBS), Daejeon 305-701, Korea and [‡]Department of Materials Science and Engineering and [§]Graduate School of Energy, Environment, Water, and Sustainability (EEWS) and Center for Nature-inspired Technology (CNiT), KAIST Institute NanoCentury, Korea Advanced Institute of Science and Technology (KAIST), Daejeon 305-701, Korea. [⊥]J.M.Y. and H.K.S. contributed equally to this work. [#]Present addresses for J.M.Y.: Department of Physics, University of California at Berkeley, California 94720, United States and Materials Sciences Division, Lawrence Berkeley National Laboratory, Berkeley, California 94720, United States.

ABSTRACT Recent real-time analyses have provided invaluable information on the volume expansion of silicon (Si) nanomaterials during their electrochemical reactions with lithium ions and have thus served as useful bases for robust design of high capacity Si anodes in lithium ion batteries (LIBs). In an effort to deepen the understanding on the critical first lithiation of Si, especially in realistic liquid environments, herein, we have engaged *in situ* graphene liquid cell transmission electron microscopy (GLC-TEM). In this technique, chemical lithiation is stimulated by electron-beam irradiation, while the lithiation process is being monitored by TEM in real time. The real-time analyses informing of the changes in the dimensions and diffraction intensity indicate that the very first lithiation of Si nanoparticle shows anisotropic volume expansion favoring the ⟨110⟩ directions due to the smaller Li diffusion energy barrier at the Si−electrolyte interface along such directions. Once passing this initial volume expansion stage, however, Li diffusion rate becomes isotropic in the inner region of the Si nanoparticle. The current study suggests that the *in situ* GLC-TEM technique can be a useful tool in understanding battery reactions of various active materials, particularly those whose initial lithiation plays a pivotal role in overall electrochemical performance and structural stability of the active materials.

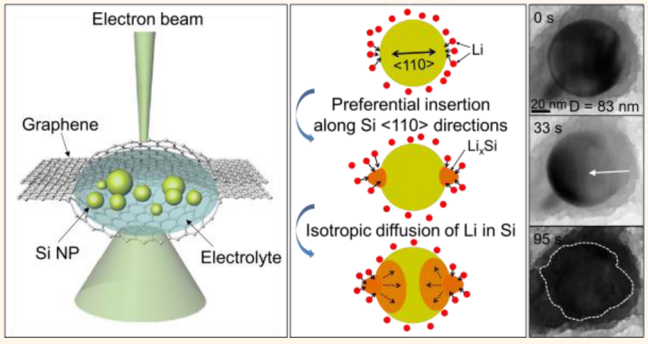

KEYWORDS: anisotropic volume expansion · lithium-ion battery · graphene liquid cell electron microscopy · chemical lithiation · silicon nanoparticle

Lithium ion batteries (LIBs) have penetrated profoundly into our everyday lives. They are powering portable electronic devices and electrified vehicles (EVs). Nevertheless, LIBs are encountering the next-level demand on further increase of the energy density, as advanced portable electronics require higher energy consumption, and the driving distance of EVs available upon each refuel is still below the customer's expectation.[1−5] In an attempt to meet such ever-growing demand with regard to the energy density, the battery community has invested significant efforts to the research of silicon (Si) anodes because the unparalleled specific capacity of Si near 4000 mA h g^{-1} can play a key role in bringing the high energy density LIBs to a reality.[5−7] Despite this attractive feature associated with the specific capacity, Si suffers from insufficient cycle life originating from its extraordinarily large volume change reaching ∼300% between the charged and discharged states.[7,8] During repeated cycles, the volume change triggers fatal capacity fading mechanisms, including pulverization of the active material, film delamination, contact loss between Si and carbon conducting agents, and unstable solid-electrolyte interphase (SEI) formation.[9−12] Hence, fundamental understanding of the volume expansion of Si during lithiation, especially in the first cycle, is essential in robust electrode design.

To this end, a vast number of experimental[7−26] and theoretical[27−32] investigations

* Address correspondence to j.y.lee@kaist.ac.kr, jangwookchoi@kaist.ac.kr.

Received for review May 21, 2014 and accepted June 30, 2014.

Published online June 30, 2014
10.1021/nn502779n

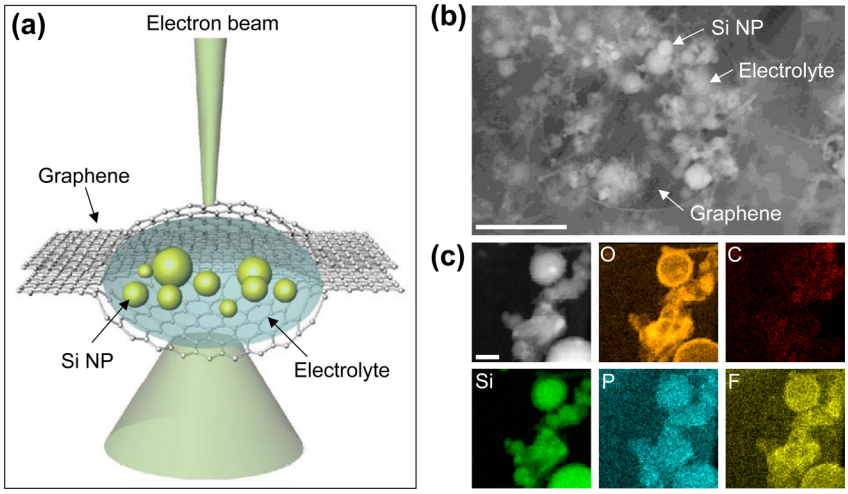

Figure 1. GLC-TEM. (a) Schematic illustration of GLC-TEM analyses. Si NPs are immersed in the liquid electrolyte, while the volume expansion of each Si NP is monitored in real-time. (b) SEM image of the GLC showing two graphene sheets containing the Si NPs and electrolyte. The whole assembly is on a holey amorphous carbon TEM grid. The scale bar is 1 μm. (c) Scanning TEM image and EDS elemental mapping of O (orange), C (red), Si (green), P (blue), and F (yellow) in the GLC. The scale bar is 100 nm.

have been recently carried out, and as a result, the knowledge on the volume expansion of Si has been substantially deepened. In particular, the *in situ* (or semi-*in situ*) transmission electron microscopy (TEM) technique has contributed markedly along this direction, as the technique allows for tracking morphological and structural changes of a single identical object throughout electrochemical processes in atomic resolution. For example, with the use of the *in situ* TEM technique, crack propagation in microsized particles,[16,20] preferential volume expansion along [110] direction,[15] and ledge-mediated migration of sharp phase boundary at the amorphous/crystalline interface[23] were elucidated based on dynamic atomic rearrangements. Although these results represent significant progresses in understanding electrochemical reactions of Si, most of the analyses were based on the use of low volatile ionic liquid electrolytes to accommodate the *in situ* cells in high vacuum TEM environments, leaving certain gaps before realistic cell conditions.[20−22,25,26,33−35] On the other hand, in the Si morphology viewpoint, while a variety of nanostructures have proven to be effective for stable cycling,[7,8,12,16,36−38] nanoparticle (NP) has been exclusively counted as a feasible active material for practical manufacturing so far because other morphological Si relies on complicated synthetic procedures that often bring cost rise together. The investigation of Si NPs, however, imposes an obstacle in the *in situ* TEM analysis, as the electric connection to a single NP is nontrivial to install in TEM cells. Also, NPs may not tend to stay at the same spots all the time during repeated large volume changes, granting another difficulty. Nevertheless, the *in situ* characterization of Si NPs in a single particle level would be highly desirable since the previous observations, such as the preferential volume expansion along the certain crystal orientation, imply that the volume expansion of NPs during lithiation could be based on a distinct structural behavior not observable with the nanowire geometry and could therefore bring novel insights unique in the particle morphology.

To investigate the lithiation dynamics of more practically viable Si NPs, the present study employed *in situ* graphene liquid cell transmission electron microscopy (GLC-TEM) technique.[39−41] The GLC-TEM technique has offered exceptional opportunities in unveiling atomic-level phenomena of nanocrystal growth[39] and biomolecular motion[40,41] in liquid environments, as liquid containing reactants can remain trapped between two graphene sheets even inside a high vacuum TEM chamber. In the current case, electron-beam (e-beam) can facilitate chemical lithiation of Si NPs entrapped in the GLC. Thus, the lithiation of Si NPs can be achieved in the actual liquid electrolyte conditions while the NPs are visualized in real time by TEM. Also, single-layer graphene sheets should not participate in reaction with Li ions because the graphene grown by chemical vapor deposition (CVD) process should be free of functional groups that allow for Li ion binding. This unique characterization capability revealed novel phenomena during lithiation of Si NPs, such as preferential lithiation onset along certain crystal orientations followed by isotropic Li diffusion in the inner regions of Si NPs, which has been unseen from the previous *in situ* analyses.

RESULTS AND DISCUSSION

Figure 1a schematically represents GLC-TEM in which Si NPs are immersed in the liquid electrolyte. For preparation of this cell, similarly to the previous reports,[39,42] liquid electrolyte (1 M of lithium hexafluorophosphate ($LiPF_6$) in solvent mixture consisting of ethylene carbonates (EC), dimethyl carbonates (DMC), and diethyl carbonates (DEC) in a 1:1:1 volumetric ratio)

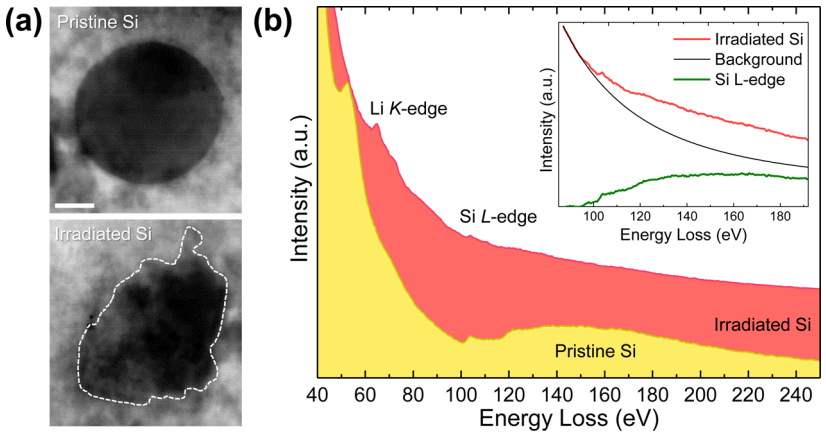

Figure 2. Chemical lithiation of Si NPs in the GLC by electron-beam irradiation. (a) Bright-field TEM images showing morphological change of the same Si NP in the GLC before and after the e-beam irradiation for 600 s. The scale bar is 50 nm. (b) EELS obtained from the pristine (yellow line) and electron-beam irradiated Si NPs (red line), respectively. Inset shows a Si *L*-edge signal (green line) acquired by extracting background (black line) from the spectrum of the irradiated Si NP (red line).

containing Si NPs was first dropped on a CVD grown graphene sheet. The second graphene sheet was transferred onto the first one followed by suction of the liquid electrolyte. After the suction process, the graphene sheets became sealed *via* van der Waals interaction through the spots where the electrolyte was removed. But a small amount of the liquid electrolyte still remained trapped between the two graphene sheets. The number of particles in each graphene pocket was varied depending on graphene size, but it was usually in the range of 5−30. A graphene liquid cell sample fabricated on a TEM grid with millimeter size has tens of graphene pockets. Among them, at least several graphene pockets contain appropriate amounts of particles and electrolyte for TEM observation. Focused e-beam was irradiated onto the Si NPs and electrolyte in the GLC to initiate the chemical lithiation. Figure 1b displays a scanning electron microscopy (SEM) image of the fabricated GLC composed of two graphene sheets encapsulating Si NPs and the liquid electrolyte. Blurred white contrast indicates graphene sheets with the liquid electrolyte entrapped. Figure 1c shows elemental mapping of oxygen (O), carbon (C), Si, phosphorus (P), and fluorine (F) using energy-dispersive X-ray spectroscopy (EDS). The contents of O, C, P, and F were detected over the entire measurement area of GLC including Si NPs, verifying complete immersion of Si NPs in the liquid electrolyte. The EDS mapping showed especially higher concentrations of O, C, P, and F over the Si NPs, which is presumably due to SEI formation.[43] By contrast, the C concentration was distributed more homogeneously over the entire area because of the covering graphene sheets. In our analyses, Si NPs were not being moved so the imaging was steadily processed.

Figure 2a shows bright-field TEM images of an identical Si NP (diameter = 80 nm) immersed in electrolyte before and after e-beam irradiation for 600 s. After this irradiation, the smooth surface of the Si NP became rougher with a relatively unclear surface boundary (white dotted line). This morphology change is the first evidence of the chemical lithiation of Si facilitated by the e-beam irradiation. In a control test where the same dose of e-beam was used for Si NPs not encapsulated in the liquid electrolyte or in the salt-free electrolyte, morphology change was not observed at all (Supporting Information Figure S1). Figure 2b displays electron energy-loss spectra (EELS) of the Si NPs before and after the e-beam irradiation. Compared to the spectrum of the pristine Si (yellow colored), the sharp Li *K*-edge near 60 eV was newly detected due to Li insertion into Si NP as well as its surrounding electrolyte after the e-beam irradiation. More direct evidence for the Li insertion into Si NP is the blurred Si *L*-edge in the range of 99−140 eV. Figure 2b inset clearly shows the blurred Si *L*-edge after the baseline subtraction and reflects the diluted Si signal in the amorphous Li_xSi phase.[15] From the further TEM analysis (Supporting Information Figure S2), it was found that the $LiPF_6$ salt can be decomposed and crystallized into LiF and PF_5 in the electrolyte.[24,44,45] The decomposition can progress further to produce Li atoms by e-beam irradiation.[46] As evidenced in the previous studies,[14−16] it is anticipated that the Li atoms distribute homogeneously on the NP surfaces utilizing their very fast surface diffusion on the Si, and the lithiation of Si takes place spontaneously due to the well-known high reactivity between both elements.[33] Although the e-beam-induced chemical lithiation kinetics may not be identical to that of the electrochemical lithiation, the current chemical lithiation fairly simulates structural evolution during electrochemical lithiation and is thus useful in understanding the volume expansion of Si NPs.[16,35]

More quantitative analyses were performed for multiple Si NPs, especially focusing on the volume expansion in different crystal orientations (Figure 3). For the representative three Si NP cases (Figure 3a−c

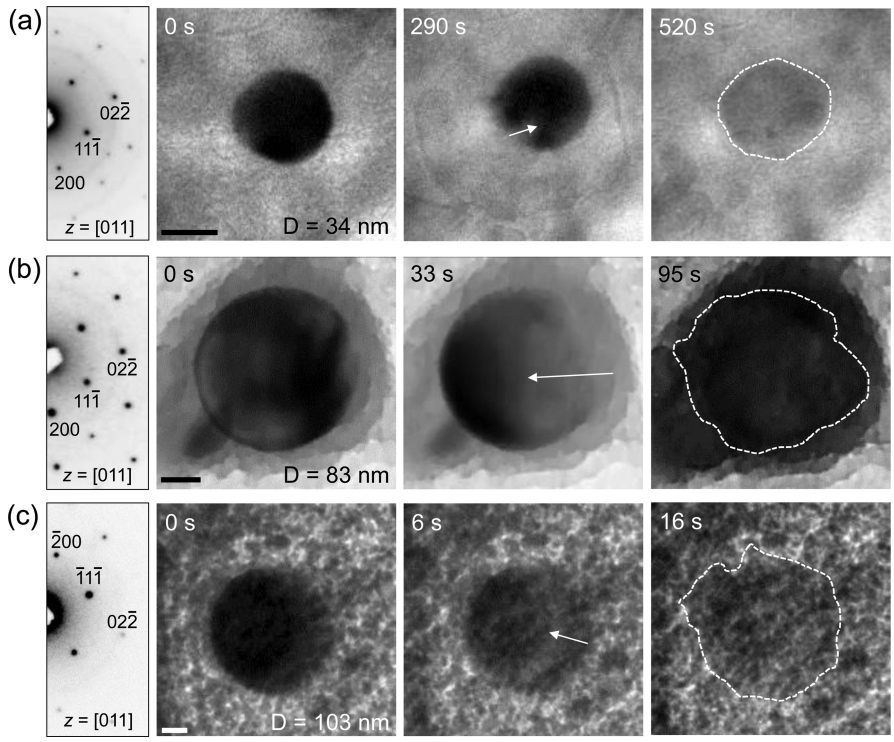

Figure 3. Morphological and dimensional changes of Si NPs analyzed by GLC-TEM during the course of lithiation. (a−c) Time-series bright-field TEM images of the Si NPs with initial diameters of 34, 83, and 103 nm, respectively. The white arrows indicate the Si⟨110⟩ directions. The SA-EDPs in (a−c) indicate crystalline nature of the pristine Si NPs and their crystallographic orientations along ⟨110⟩ zone axes. The scale bars in (a−c) are 20 nm.

and Supporting Information Movies S1−S3) where their original diameters are 34, 83, and 103 nm, we monitored morphological and dimensional changes along the ⟨110⟩, ⟨111⟩, and ⟨100⟩ directions. The selected-area electron diffraction patterns (SA-EDPs) (the left ones in Figure 3a−c) indicate that all of the three Si NPs are single-crystalline with ⟨110⟩ zone axes. The most noticeable feature during initial lithiation of all the three NPs is that the lithiation progresses predominantly along the ⟨110⟩ directions leading to the anisotropic volume expansion along the same crystal orientations, as indicated by the white arrows in Figure 3a−c. In separate analyses (Supporting Information Figure S3) where the Si zone axes were aligned along the ⟨111⟩ directions, the predominant lithiation along the ⟨110⟩ directions resulted in an isotropically expanded image of the given Si NP. This anisotropic volume expansion is commensurate with the previous observations.[15,17−19]

For more quantitative understanding, the dimensional changes of each Si NP were plotted for the ⟨110⟩, ⟨111⟩, and ⟨100⟩ directions at different irradiation times (Figure 4a−c). The dimensional changes in all of the NP cases unanimously confirmed the preferred initial lithiation in the ⟨110⟩ directions after certain incubation times for sufficient Li supply, as all of them exhibited the earlier onset points for the ⟨110⟩ curves. The onset point corresponds to the very first moment where the volume begins to expand, and those points for all of the three orientations are denoted as arrows in Figure 4a−c for clarity. The preferred lithiation in the ⟨110⟩ directions at the very early lithiation stage can be explained by the lower energy barriers (∼0.50 eV) for subsurface diffusion of Li at the Si-electrolyte interfaces along such orientations.[28,29] Interestingly, once passing the onset points, the dimensions in all of the orientations increased in similar rates (similar slopes), which implies isotropic diffusion without any preferred orientations, and these phenomena were observed for all of the NP cases (Figure 4d). Also, the lithiation speed can be extracted from the dimensional change of Si NP because the volume expansion by the formation of the amorphous Li_xSi phase reflects the diffusion rate of the phase boundary at the bare Si-amorphous Li_xSi interface. The average rate of the dimensional increase was 0.5 nm/s, which is indeed smaller than previously reported value of 2.3 nm/s in intrinsic Si nanowires,[47] perhaps due to the absence of electrical bias. Combining these results, we conclude that the very first lithiation at the Si-electrolyte interface has the strong orientation dependence favoring the ⟨110⟩ directions, but once the lithiation passes this initial stage, Li diffusion occurs isotropically, regardless of the NP size.

The isotropic Li diffusion in crystalline Si is also aligned well with the classical view.[28,48] In the classical view, Li diffusivity was explained based on the distance between adjacent interstitial sites and the diffusion

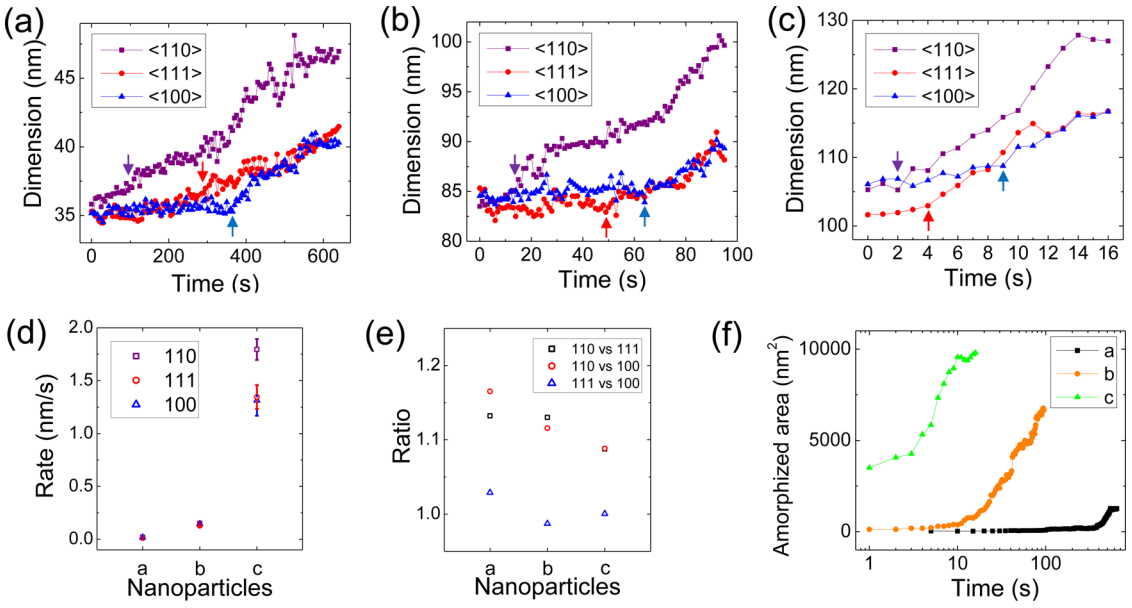

Figure 4. Dimensional and areal dynamics of Si NPs during the course of lithiation. (a–c) The dimensional changes of the Si NPs along various crystallographic directions as a function of the irradiation time. The purple, red, and blue arrows indicate the onset points of the dimensional increases along the ⟨110⟩, ⟨111⟩, and ⟨100⟩ directions, respectively. (d) The rates of the dimensional increases along the different crystallographic directions. (e) The ratios of the lithiated NP dimensions in the different crystallographic directions when measured at the end of the characterizations shown in (a–c). (f) The amorphized areas as a function of the irradiation time. All the results in this figure were attained from the three Si NPs in Figure 3a–c.

barrier. In the bulk crystalline Si, it has been known that the diffusion barrier is ~0.65 eV regardless of the crystal orientation.[49] Although the adjacent tetrahedral distances are different depending on the crystal orientation, the difference is not to a level making a drastic change in the diffusivity. To the best of our knowledge, this isotropic diffusion after the onset of lithiation has never been observed in real time, which is attributed to the limited sample geometry in the previous *in situ* TEM studies. That is, the previous studies dealt mostly with Si nanowires so that only the radial dimensional changes were mainly characterized, and dimensional changes in other directions were difficult to follow. The distinct initial lithiation also resulted in different dimensional changes along the different crystal orientations. For the three Si NPs, the dimensional increments were 31%, 19%, and 21% along the ⟨110⟩ directions, whereas the values dropped to 18%, 3%, and 15%, and 15%, 6%, and 10% along the ⟨111⟩ and ⟨100⟩ directions, respectively. Figure 4e shows the deformation anisotropy measured by the ratio of the lithiated NP dimension in different crystallographic directions. The average ratio of expanded dimension is 1.12 between ⟨110⟩ and ⟨111⟩ or ⟨100⟩ directions, which is smaller than fully lithiated Si nanowires,[15,17] and 1.01 between ⟨111⟩ and ⟨100⟩ directions, which is due to similar lithiation onset points. Figure 4f shows the increments of cross-sectional amorphized area in the NP with time. The amorphized area increases with dimension increments and the total increases with respect to the original values were 33%, 23%, and 15%, respectively, for the three Si NPs, which are also smaller than those expected for full lithiation.[17] These lesser degrees of lithiation might be from insufficient Li resource available around the Si NPs. Nonetheless, the rate-limiting initial lithiation discussed herein should be valid, as such phenomenon is independent of the degree of lithiation. This incomplete lithiation also explains why the larger Si NPs showed smaller volume expansion ratios in Figures 4f.

The orientation-dependent initial lithiation was also supported by electron diffraction analyses (Figure 5). SA-EDPs were obtained for a single-crystalline Si NP (diameter = 60 nm) as the lithiation progressed. These analyses are useful in monitoring the orientation-dependent lithiation because the diffraction intensities corresponding to all the relevant crystal orientations can be quantified throughout the entire lithiation. Figure 5a shows the SA-EDPs of an identical Si NP with the ⟨110⟩ zone axis at various lithiation durations (Movie S4). Three main diffraction spots assigned to the ⟨220⟩, ⟨111⟩, and ⟨200⟩ crystal orientations were detected, and the intensities of these spots gradually decreased as the e-beam irradiation continues, once again an outcome of the amorphization of Si. This diffraction fading was quantitatively plotted for the ⟨220⟩ and ⟨111⟩ orientations in Figure 5b. The ⟨200⟩ spots were omitted because those spots could also originate from double diffraction of the {111} planes in the diamond cubic structure. Consistent with the dimensional change results in Figure 4a–c, the intensity of the ⟨220⟩ spot began to decrease earlier than that of the ⟨111⟩ spot. The onset for the diffraction

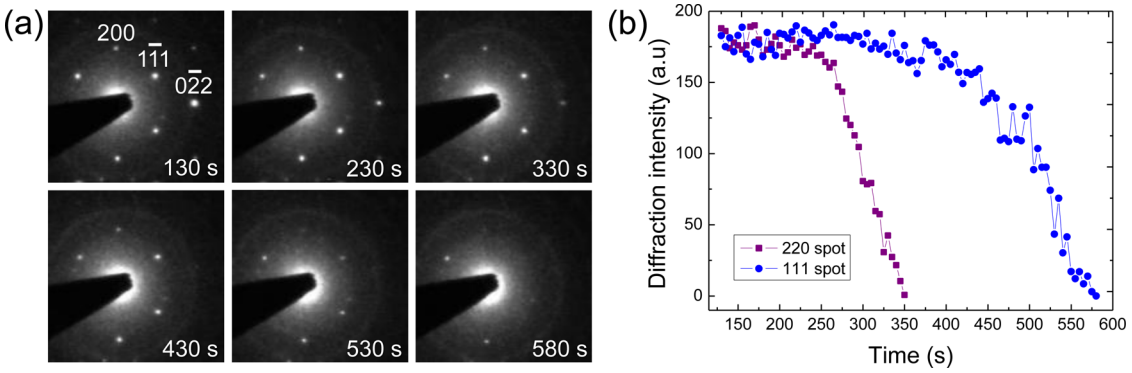

Figure 5. Lithiation-induced anisotropic amorphization of a single-crystalline Si NP. (a) Time-series SA-EDPs of the single Si NP with ⟨110⟩ zone axis. (b) The intensity changes of the diffraction spots as a function of the irradiation time: the {220} planes (purple square) and the {111} planes (blue sphere).

fading was approximately 260 and 440 s for the ⟨220⟩ and ⟨111⟩ orientations, respectively, reconfirming the preferential initial lithiation along the ⟨110⟩ directions. Figure 5b also consistently exhibits that after the onset points, the diffraction intensities of both orientations decayed at almost the same rates, which appears to be reflective of the isotropic Li diffusion in the inner region of Si. In addition, it should be noted that in our analyses based on TEM images and SA-EDPs, the incubation time before the lithiation onset could be varied depending on the e-beam dose and other miscellaneous experimental conditions. However, the anisotropic onset trend among the crystalline orientations and the amorphization rate were attained for all the particles whose crystallographic orientations are aligned with e-beam direction and are independent of such experimental conditions because those phenomena are relevant to the lithiation process after the onset points.

CONCLUSION

In summary, we demonstrate that *in situ* GLC-TEM can be applied for observation of real-time lithiation in Si NPs. Through these analyses, it was observed that the initial lithiation occurs preferentially along the ⟨110⟩ directions, but once the reaction front passes this initial barrier, the Li diffusion progresses isotropically, indicating that the rate-limiting diffusion barrier, which is different based on the orientations, is at Si−electrolyte interfaces rather than within the Si crystal or at interfaces between lithiated and unlithiated regions. The understanding attained from the current study can serve as a solid basis in designing high capacity Si anodes based on scalable NP active materials.

METHODS

Sample Preparation. We have fabricated the GLCs encapsulating Si NPs (Sigma-Aldrich, powder form, diameter = 20−200 nm) and standard electrolyte, 1 M lithium hexafluorophosphate ($LiPF_6$) dissolved in carbonate solvent mixture in which ethylene carbonates (EC), dimethyl carbonates (DMC), and diethyl carbonates (DEC) were occupied in a 1:1:1 volumetric ratio, following a previous report.[39] All of the GLC fabrication processes were conducted in an Ar-filled glovebox where the moisture and oxygen concentrations were kept below 1 ppm to prevent the electrolyte degradation. The prepared sample on a TEM grid was located inside a TEM holder, and the holder was quickly loaded into the TEM chamber with unavoidable minimal exposure to air for a few seconds.

Real-Time TEM Imaging. Conventional TEM (JEM-3010, 300 kV, JEOL) with a fast responding charge-coupled device (CCD) camera (SC200, Gatan) was employed for the real-time observation of lithiation process of Si NPs. The electron-beam dosage for real-time imaging was set to 500−4000 pA cm^{-2} under the observing magnification range at an accelerating voltage of 300 kV in order to initiate the electron-beam-induced chemical reaction.

EELS and EDS Measurements. EELS spectra were obtained using an Enfina spectrometer (Gatan) equipped in ARM-200F microscope (JEOL) at a 200 kV accelerating voltage condition. EDS elemental mapping was performed using Titan G2 microscope (FEI) at a 300 kV accelerating voltage condition. The both EELS and EDS measurements were conducted in the diffraction mode.

Conflict of Interest: The authors declare no competing financial interest.

Supporting Information Available: Additional *in situ* TEM data and movies. This material is available free of charge via the Internet at http://pubs.acs.org.

Acknowledgment. This work was supported by Institute for Basic Science (IBS) [IBS-R004-G3-2014-a00]. J.W.C. acknowledges financial support by the National Research Foundation of Korea (NRF) grant funded by the Korea government (MEST) (NRF-2012-R1A2A1A01011970).

REFERENCES AND NOTES

1. Tarascon, J.-M.; Armand, M. Issues and Challenges Facing Rechargeable Lithium Batteries. *Nature* **2001**, *414*, 359–367.
2. Scrosati, B. Challenge of Portable Power. *Nature* **1995**, *373*, 557–558.
3. Armand, M.; Tarascon, J.-M. Building Better Batteries. *Nature* **2008**, *451*, 652–657.
4. Gu, M.; Belharouak, I.; Genc, A.; Wang, Z.; Wang, D.; Amine, K.; Gao, F.; Zhou, G.; Thevuthasan, S.; Baer, D. R.; *et al.* Conflicting Roles of Nickel in Controlling Cathode Performance in Lithium Ion Batteries. *Nano Lett.* **2012**, *12*, 5186–5191.

5. McDowell, M. T.; Lee, S. W.; Nix, W. D.; Cui, Y. 25th Anniversary Article: Understanding the Lithiation of Silicon and Other Alloying Anodes for Lithium-Ion Batteries. *Adv. Mater.* **2013**, *25*, 4966–4985.
6. Kasavajjula, U.; Wang, C.; Appleby, A. J. Nano- and Bulk-Silicon–Based Insertion Anodes for Lithium-Ion Secondary Cells. *J. Power Sources* **2007**, *163*, 1003–1039.
7. Kovalenko, I.; Zdyrko, B.; Magasinski, A.; Hertzberg, B.; Milicev, Z.; Burtovyy, R.; Luzinov, I.; Yushin, G. A Major Constituent of Brown Algae for Use in High-Capacity Li-Ion Batteries. *Science* **2011**, *334*, 75–79.
8. Chan, C. K.; Peng, H.; Liu, G.; McIlwrath, K.; Zhang, X. F.; Huggins, R. A.; Cui, Y. High-Performance Lithium Battery Anodes Using Silicon Nanowires. *Nat. Nanotechnol.* **2008**, *3*, 31–35.
9. Xie, J.; Yang, X.; Zhou, S.; Wang, D. Comparing One- and Two-Dimensional Heteronanostructures as Silicon-Based Lithium Ion Battery Anode Materials. *ACS Nano* **2011**, *5*, 9225–9231.
10. Chen, Z.; Christensen, L.; Dahn, J. R. Large-Volume-Change Electrodes for Li-Ion Batteries of Amorphous Alloy Particles Held by Elastomeric Tethers. *Electrochem. Commun.* **2003**, *5*, 919–923.
11. Key, B.; Bhattacharyya, R.; Morcrette, M.; Seznéc, V.; Tarascon, J.-M.; Grey, C. P. Real-Time NMR Investigations of Structural Changes in Silicon Electrodes for Lithium-Ion Batteries. *J. Am. Chem. Soc.* **2009**, *131*, 9239–9249.
12. Wu, H.; Chan, G.; Choi, J. W.; Ryu, I.; Yao, Y.; McDowell, M. T.; Lee, S. W.; Jackson, A.; Yang, Y.; Hu, L.; *et al.* Stable Cycling of Double-Walled Silicon Nanotube Battery Anodes through Solid–Electrolyte Interphase Control. *Nat. Nanotechnol.* **2012**, *7*, 310–315.
13. Huang, J. Y.; Zhong, L.; Wang, C. M.; Sullivan, J. P.; Xu, W.; Zhang, L. Q.; Mao, S. X.; Hudak, N. S.; Liu, X. H.; Subramanian, A.; *et al. In Situ* Observation of the Electrochemical Lithiation of a Single SnO_2 Nanowire Electrode. *Science* **2010**, *330*, 1515–1520.
14. McDowell, M. T.; Lee, S. W.; Wang, C.; Cui, Y. The Effect of Metallic Coatings and Crystallinity on the Volume Expansion of Silicon during Electrochemical Lithiation/Delithiation. *Nano Energy* **2012**, *1*, 401–410.
15. Liu, X. H.; Zheng, H.; Zhong, L.; Huang, S.; Karki, K.; Zhang, L. Q.; Liu, Y.; Kushima, A.; Liang, W. T.; Wang, J. W.; *et al.* Anisotropic Swelling and Fracture of Silicon Nanowires during Lithiation. *Nano Lett.* **2011**, *11*, 3312–3318.
16. Liu, X. H.; Zhong, L.; Huang, S.; Mao, S. X.; Zhu, T.; Huang, J. Y. Size-Dependent Fracture of Silicon Nanoparticles during Lithiation. *ACS Nano* **2012**, *6*, 1522–1531.
17. Lee, S. W.; McDowell, M. T.; Choi, J. W.; Cui, Y. Anomalous Shape Changes of Silicon Nanopillars by Electrochemical Lithiation. *Nano Lett.* **2011**, *11*, 3034–3039.
18. Lee, S. W.; McDowell, M. T.; Berla, L. A.; Nix, W. D.; Cui, Y. Fracture of Crystalline Silicon Nanopillars during Electrochemical Lithium Insertion. *Proc. Natl. Acad. Sci. U.S.A.* **2012**, *109*, 4080–4085.
19. Goldman, J. L.; Long, B. R.; Gewirth, A. A.; Nuzzo, R. G. Strain Anisotropies and Self-Limiting Capacities in Single-Crystalline 3D Silicon Microstructures: Models for High Energy Density Lithium-Ion Battery Anodes. *Adv. Funct. Mater.* **2011**, *21*, 2412–2422.
20. Ghassemi, H.; Au, M.; Chen, N.; Heiden, P. A.; Yassar, R. S. *In Situ* Electrochemical Lithiation/Delithiation Observation of Individual Amorphous Si Nanorods. *ACS Nano* **2011**, *5*, 7805–7811.
21. Wang, C.-M.; Li, X.; Wang, Z.; Xu, W.; Liu, J.; Gao, F.; Kovarik, L.; Zhang, J.-G.; Howe, J.; Burton, D. J.; *et al. In Situ* TEM Investigation of Congruent Phase Transition and Structural Evolution of Nanostructured Silicon/Carbon Anode for Lithium Ion Batteries. *Nano Lett.* **2012**, *12*, 1624–1632.
22. Gu, M.; Parent, L. R.; Mehdi, B. L.; Unocic, R. R.; McDowell, M. T.; Sacci, R. L.; Xu, W.; Connell, J. G.; Xu, P.; Abellan, P.; *et al.* Demonstration of an Electrochemical Liquid Cell for Operando Transmission Electron Microscopy Observation of the Lithiation/Delithiation Behavior of Si Nanowire Battery Anodes. *Nano Lett.* **2013**, *13*, 6106–6112.
23. Liu, X. H.; Wang, J. W.; Huang, S.; Fan, F.; Huang, X.; Liu, Y.; Krylyuk, S.; Yoo, J.; Dayeh, S. A.; Davydov, A. V.; *et al. In Situ* Atomic-Scale Imaging of Electrochemical Lithiation in Silicon. *Nat. Nanotechnol.* **2012**, *7*, 749–756.
24. Abellan, P.; Mehdi, B. L.; Parent, L. R.; Gu, M.; Park, C.; Xu, W.; Zhang, Y.; Arslan, I.; Zhang, J.-G.; Wang, C.-M.; *et al.* Probing the Degradation Mechanisms in Electrolyte Solutions for Li-Ion Batteries by *in Situ* Transmission Electron Microscopy. *Nano Lett.* **2014**, *14*, 1293–1299.
25. Holtz, M. E.; Yu, Y.; Gunceler, D.; Gao, J.; Sundararaman, R.; Schwarz, K. A.; Arias, T. A.; Abruña, H. D.; Muller, D. A. Nanoscale Imaging of Lithium Ion Distribution during *in Situ* Operation of Battery Electrode and Electrolyte. *Nano Lett.* **2014**, *14*, 1453–1459.
26. Zeng, Z.; Liang, W.-I.; Liao, H.-G.; Xin, H. L.; Chu, Y.-H.; Zheng, H. Visualization of Electrode–Electrolyte Interfaces in $LiPF_6$/EC/DEC Electrolyte for Lithium Ion Batteries *via in Situ* TEM. *Nano Lett.* **2014**, *14*, 1745–1750.
27. Jung, S. C.; Choi, J. W.; Han, Y.-K. Anisotropic Volume Expansion of Crystalline Silicon during Electrochemical Lithium Insertion: An Atomic Level Rationale. *Nano Lett.* **2012**, *12*, 5342–5347.
28. Chan, M. K. Y.; Wolverton, C.; Greeley, J. P. First Principles Simulations of the Electrochemical Lithiation and Delithiation of Faceted Crystalline Silicon. *J. Am. Chem. Soc.* **2012**, *134*, 14362–14374.
29. Cubuk, E. D.; Wang, W. L.; Zhao, K.; Vlassak, J. J.; Suo, Z.; Kaxiras, E. Morphological Evolution of Si Nanowires upon Lithiation: A First-Principles Multiscale Model. *Nano Lett.* **2013**, *13*, 2011–2015.
30. Zhao, K.; Wang, W. L.; Gregoire, J.; Pharr, M.; Suo, Z.; Vlassak, J. J.; Kaxiras, E. Lithium-Assisted Plastic Deformation of Silicon Electrodes in Lithium-Ion Batteries: A First-Principles Theoretical Study. *Nano Lett.* **2011**, *11*, 2962–2967.
31. Pharr, M.; Zhao, K.; Wang, X.; Suo, Z.; Vlassak, J. J. Kinetics of Initial Lithiation of Crystalline Silicon Electrodes of Lithium-Ion Batteries. *Nano Lett.* **2012**, *12*, 5039–5047.
32. Zhao, K.; Pharr, M.; Wan, Q.; Wang, W. L.; Kaxiras, E.; Vlassak, J. J.; Suo, Z. Concurrent Reaction and Plasticity during Initial Lithiation of Crystalline Silicon in Lithium-Ion Batteries. *J. Electrochem. Soc.* **2012**, *159*, A238–A243.
33. Liu, X. H.; Liu, Y.; Kushima, A.; Zhang, S.; Zhu, T.; Li, J.; Huang, J. Y. *In Situ* TEM Experiments of Electrochemical Lithiation and Delithiation of Individual Nanostructures. *Adv. Energy Mater.* **2012**, *2*, 722–741.
34. Zhong, L.; Liu, X. H.; Wang, G. F.; Mao, S. X.; Huang, J. Y. Multiple-Stripe Lithiation Mechanism of Individual SnO_2 Nanowires in a Flooding Geometry. *Phys. Rev. Lett.* **2011**, *106*, 248302.
35. Liu, X. H.; Huang, J. Y. *In Situ* TEM Electrochemistry of Anode Materials in Lithium Ion Batteries. *Energy Environ. Sci.* **2011**, *4*, 3844–3860.
36. Hwang, T. H.; Lee, Y. M.; Kong, B.-S.; Seo, J.-S.; Choi, J. W. Electrospun Core–Shell Fibers for Robust Silicon Nanoparticle-Based Lithium Ion Battery Anodes. *Nano Lett.* **2012**, *12*, 802–807.
37. Magasinski, A.; Dixon, P.; Hertzberg, B.; Kvit, A.; Ayala, J.; Yushin, G. High-Performance Lithium-Ion Anodes Using a Hierarchical Bottom-Up Approach. *Nat. Mater.* **2010**, *9*, 353–358.
38. Song, T.; Xia, J.; Lee, J.-H.; Lee, D. H.; Kwon, M.-S.; Choi, J.-M.; Wu, J.; Doo, S. K.; Chang, H.; Park, W. I.; *et al.* Arrays of Sealed Silicon Nanotubes as Anodes for Lithium Ion Batteries. *Nano Lett.* **2010**, *10*, 1710–1716.
39. Yuk, J. M.; Park, J.; Ercius, P.; Kim, K.; Hellebusch, D. J.; Crommie, M. F.; Lee, J. Y.; Zettl, A.; Alivisatos, A. P. High-Resolution EM of Colloidal Nanocrystal Growth Using Graphene Liquid Cells. *Science* **2012**, *336*, 61–64.
40. Chen, Q.; Smith, J. M.; Park, J.; Kim, K.; Ho, D.; Rasool, H. I.; Zettl, A.; Alivisatos, A. P. 3D Motion of DNA-Au Nanoconjugates in Graphene Liquid Cell Electron Microscopy. *Nano Lett.* **2013**, *13*, 4556–4561.
41. Wang, C.; Qiao, Q.; Shokuhfar, T.; Klie, R. F. High-Resolution Electron Microscopy and Spectroscopy of Ferritin in

Biocompatible Graphene Liquid Cells and Graphene Sandwiches. *Adv. Mater.* **2014**, 10.1002/adma.201306069.
42. Yuk, J. M.; Kim, K.; Alemán, B.; Regan, W.; Ryu, J. H.; Park, J.; Ercius, P.; Lee, H. M.; Alivisatos, A. P.; Crommie, M. F.; *et al.* Graphene Veils and Sandwiches. *Nano Lett.* **2011**, *11*, 3290–3294.
43. Lee, Y. M.; Lee, J. Y.; Shim, H.-T.; Lee, J. K.; Park, J.-K. SEI Layer Formation on Amorphous Si Thin Electrode during Precycling. *J. Electrochem. Soc.* **2007**, *154*, A515–A519.
44. Xu, K. Nonaqueous Liquid Electrolytes for Lithium-Based Rechargeable Batteries. *Chem. Rev.* **2004**, *104*, 4303–4417.
45. Sloop, S. E.; Pugh, J. K.; Wang, S.; Kerr, J. B.; Kinoshita, K. Chemical Reactivity of PF_5 and $LiPF_6$ in Ethylene Carbonate/Dimethyl Carbonate Solutions. *Electrochem. Solid-State Lett.* **2001**, *4*, A42–A44.
46. Ghatak, J.; Guan, W.; Möbus, G. *In Situ* TEM Observation of Lithium Nanoparticle Growth and Morphological Cycling. *Nanoscale* **2012**, *4*, 1754–1759.
47. Liu, X. H.; Zhang, L. Q.; Zhong, L.; Liu, Y.; Zheng, H.; Wang, J. W.; Cho, J.-H.; Dayeh, S. A.; Picraux, S. T.; Sullivan, J. P.; *et al.* Ultrafast Electrochemical Lithiation of Individual Si Nanowire Anodes. *Nano Lett.* **2011**, *11*, 2251–2258.
48. Nye, J. F. *Physical Properties of Crystals: Their Representation by tensors and Matrices*; Oxford University Press: Oxford, U.K., 1957.
49. Lide, D. R., Ed. *CRC Handbook of Chemistry and Physics*; CRC Press: Boca Raton, FL, 2004; pp 12−108.